ARTICLE   OPEN

Check for updates

Co-benefits of reducing PM$_{2.5}$ and improving visibility by COVID-19 lockdown in Wuhan

Liquan Yao[1,2], Shaofei Kong [1,2,3 ✉], Huang Zheng [1,2], Nan Chen[3,4], Bo Zhu[3,4], Ke Xu[3,4], Wenxiang Cao[3,4], Ying Zhang[1], Mingming Zheng[1,2], Yi Cheng[1,2], Yao Hu[1,2], Zexuan Zhang[1,2], Yingying Yan[1], Dantong Liu[5], Tianliang Zhao[6], Yongqing Bai[7] and Shihua Qi[2]

The less improvement of ambient visibility suspects the government's efforts on alleviating PM$_{2.5}$ pollution. The COVID-19 lockdown reduced PM$_{2.5}$ and increased visibility in Wuhan. Compared to pre-lockdown period, the PM$_{2.5}$ concentration decreased by 39.0 µg m^{-3}, dominated by NH$_4$NO$_3$ mass reduction (24.8 µg m^{-3}) during lockdown period. The PM$_{2.5}$ threshold corresponding to visibility of 10 km (PTV$_{10}$) varied in 54–175 µg m^{-3} and an hourly PM$_{2.5}$ of 54 µg m^{-3} was recommended to prevent haze occurrence. The lockdown measures elevated PTV$_{10}$ by 9–58 µg m^{-3} as the decreases in PM$_{2.5}$ mass scattering efficiency and optical hygroscopicity. The visibility increased by 107%, resulted from NH$_4$NO$_3$ extinction reduction. The NH$_4$NO$_3$ mass reduction weakened its mutual promotion with aerosol water and increased PM$_{2.5}$ deliquescence humidity. Controlling TNO$_3$ (HNO$_3$ + NO$_3^-$) was more effective to reduce PM$_{2.5}$ and improve visibility than NH$_x$ (NH$_3$ + NH$_4^+$) unless the NH$_x$ reduction exceeded 11.7–17.5 µg m^{-3}.

INTRODUCTION

Atmospheric visibility provides intuitive grasp of air quality for public[1]. China has suffered substantial visibility deterioration in the past years[2–5], which adversely impacts traffic[6] and human happiness[7]. Intensive occurrences of haze with low visibility have raised public awareness[8–12]. Since the promulgation of Air Pollution Prevention Control and Action Plan in 2013[13], the national emissions of SO$_2$, NO$_x$, and primary fine particle (PM$_{2.5}$) declined by 59, 21 and 33%, respectively[14–16]. The PM$_{2.5}$ mass concentrations in Beijing–Tianjin–Hebei, Yangtze River Delta, and Pearl River Delta reduced by 28–40% during 2013–2017[17]. However, such great mitigations in air pollution are not directly visible to the general population because the ambient visibility seems less improved, especially in winter[11,12,14,16,18,19]. For example, the frequency of low visibility events only decreased by 5% despite the reduction in PM$_{2.5}$ > 30% in 2018 in Southern China when compared with 2013[19]. This depressing visibility improvement is also found in Eastern China even though PM$_{2.5}$ has lowered by 50.8 µg m^{-3} from 2013 to 2018[16]. The annual average visibilities for Fenwei Plain and Central China are still < 10 km, and the haze days are still > 71 days[20]. All these mask the intense and painstaking efforts that the government devoted for defending the blue sky.

Aerosol light extinction (b_{ext}) including aerosol absorption (b_{ap}) and scattering (b_{sp}) was the key deciding ambient visibility[4,21]. The aerosol chemical compositions and hygroscopic properties impact b_{ext} substantially[19,22–25]. Organic matter (OM, 29–52%)[26], (NH$_4$)$_2$SO$_4$ (29%)[27], and NH$_4$NO$_3$ (31–45%)[28] were the main contributors to b_{ext} in the megacities of China. The contribution from sulfate-nitrate-ammonium (SNA) to b_{ext} even increased to

nearly 80% under polluted atmospheric conditions[22]. Typically, the haze events are associated with elevated ambient relative humidity (RH), which promotes SNA formation[29–33] and enhances b_{sp}[25,34,35]. The aerosol hygroscopicity increased b_{sp} by 1.8 times at RH of 80%, compared with that of dry conditions (RH < 40%)[36]. For improving visibility, it is pivotal to identify the key chemical components impacting b_{ext} and control their precursor gases.

Temporary emission control measures have been frequently implemented during mega-event periods, aimed at reducing the mass concentrations of PM$_{2.5}$, SO$_2$, NO$_x$, and O$_3$[24,37,38]. The mass concentrations of PM$_{2.5}$ decreased obviously by 40–49% in these events[37,38], which actuated the appearances of blue sky[37,39]. Li et al.[40] observed that the frequency of hazy days decreased to 36% during the Beijing Olympics because the b_{ext} contributions of (NH$_4$)$_2$SO$_4$ and NH$_4$NO$_3$ decreased by 17.1 and 13%, respectively. Tao et al.[41] found that the "APEC blue" was mainly raised by SNA extinction reduction (30%), with 5 days holding ambient visibility > 20 km. However, the frequency of haze occurrence increased by 7% during the 16th Asian Games period though PM$_{2.5}$ decreased by 32%[42]. The unexpected haze during the former mega-event periods implies that the temporal pollution control measures for air pollutants at a regional scale may be not effective for improving the ambient visibility necessarily.

The lockdown events due to coronavirus disease 2019 (COVID-19) provide the widest, longest, and thorough "controlled experiment," to investigate the impacts of unexpected control measures on reducing air pollutant concentrations and improving visibility. Abundant studies have reported large decreases in CO$_2$[43–45], NO$_x$[46–48], particulate matter[49–51], and associated chemical components[52–56]. While the reduced anthropogenic emissions

[1]Department of Atmospheric Sciences, School of Environmental Studies, China University of Geosciences, Wuhan, China. [2]Department of Environmental Science and Engineering, School of Environmental Studies, China University of Geosciences, Wuhan, China. [3]Research Centre for Complex Air Pollution of Hubei Province, Wuhan, China. [4]Eco-Environmental Monitoring Centre of Hubei Province, Wuhan, China. [5]Department of Atmospheric Sciences, School of Earth Sciences, Zhejiang University, Hangzhou, China. [6]Collaborative Innovation Center on Forecast and Evaluation of Meteorological Disasters, Key Laboratory for Aerosol-Cloud-Precipitation of the China Meteorological Administration, PREMIC, Nanjing University of Information Science & Technology, Nanjing, China. [7]Institute of Heavy Rain, China Meteorological Administration, Wuhan, China. ✉email: kongshaofei@cug.edu.cn

did not hold back the occurrences of severe haze events in China because of unfavorable meteorology[57,58], enhanced secondary formation[18,59], and regional transport[60,61]. In addition, the aerosol optical depth (AOD) was less affected by the reductions[47,57]. In fact, the impacts of the strictest lockdown measures on aerosol optical properties are puzzled and till now no studies have focused on this point.

Wuhan is the first locked city and the lockdown measures are the strictest. This study analyzed the online monitoring datasets including b_{sp}, b_{ap}, and chemical components for $PM_{2.5}$ in Wuhan for pre-lockdown period (PLP) and lockdown period (LP). The impacts of chemical compositions and hygroscopic growth on b_{ext} and corresponding mechanisms were investigated, and the key chemical component impacting b_{ext} was identified. Priority policies for reducing $PM_{2.5}$ and improving ambient visibility effectively were proposed. Results here can provide a reference for policy making from the view of improving ambient visibility.

RESULTS AND DISCUSSION

Substantial $PM_{2.5}$ reduction and visibility improvement
The average $PM_{2.5}$ mass concentration decreased by 37.8% in LP ($47.8 \pm 25.5\ \mu g\ m^{-3}$) compared with that for PLP ($76.8 \pm 34.0\ \mu g\ m^{-3}$, Fig. 1a), since the lockdown measures actually reduced the anthropogenic emissions[45,59,61]. The decrements in the average mass concentrations of major compounds varied from $0.8\ \mu g\ m^{-3}$ (elemental carbon (EC)) to $24.8\ \mu g\ m^{-3}$ (NH_4NO_3) except for secondary organic aerosol (SOA) (Fig. 1b). The decrease in NH_4NO_3 made up 63.6% of $PM_{2.5}$ mass reduction. The average SOA concentration showed an increase of $1.6\ \mu g\ m^{-3}$ and its mass percentage in $PM_{2.5}$ raised by 6.9%, verifying the enhanced secondary formation[18].

The mean b_{sp} and b_{ap} decreased by 39.0% ($151.2\ Mm^{-1}$) and 31.4% ($8.9\ Mm^{-1}$) during LP, respectively (Fig. 1a). The single scattering albedo decreased only by 1.1% during LP (0.91), implying the strong scattering ability of particle. The RH slightly descended by 8.8% from PLP ($78.4 \pm 13.8\%$) to LP ($71.4 \pm 15.7\%$). The visibility displayed a remarkable ($p < 0.01$) increase of 106.7% (14.4 km) during LP, demonstrating that the strict control measures were effective to improve the ambient visibility along with the decrease of $PM_{2.5}$. While in Eastern[16] and Southern China[19] the $PM_{2.5}$ substantially decreased, the ambient visibility was less improved due to its nonlinear relationship with $PM_{2.5}$[16,19,22,28].

During LP, severe haze events with ambient visibility < 10 km occurred on 3 and 5 February with the maximal b_{sp} and b_{ap} as 689.0 and $53.7\ Mm^{-1}$, respectively. The SNA contributed highest to $PM_{2.5}$ mass (66.7–67.4%) and b_{ext} (56.0–59.8%) (Supplementary Fig. 1). The haze events on 3 and 5 February were related with local accumulation and regional transport of air pollutants, respectively[60] (Supplementary Fig. 1), while the dominant chemical species of the 2 days were similar under the two different atmospheric circulations, highlighting the substantial role in improving ambient visibility by regional-joint control of the precursor gas emissions for SNA.

Increases in PTV_{10}
Figure 2a shows the non-linear responses of visibility to $PM_{2.5}$ under different RH intervals, with strong negative power function relationships ($R^2 > 0.71$, $p < 0.01$). The $PM_{2.5}$ thresholds corresponding to visibility of 10 km (PTV_{10}) varied from 54 to $175\ \mu g\ m^{-3}$ and decreased with RH increasing due to rapid hygroscopic growth of particles[27]. The spatiotemporal variabilities of PTV_{10}, e.g., 50–63 $\mu g\ m^{-3}$ in Sichuan basin in 2014[62] and $66\ \mu g\ m^{-3}$ in Wuhan during 2018 winter[28], reduced the consistency and reliability of air quality studies using a fixed visibility (10 km) to reflect the occurrence of haze without considering air pollution intensity[63]. Meanwhile, the

PTV_{10} for RH > 90% was 13–28% lower than the Chinese secondary $PM_{2.5}$ standard ($75\ \mu g\ m^{-3}$), implying that the air quality standard was not always able to keep the visibility > 10 km. Thus, a strict hourly $PM_{2.5}$ standard value should be emphasized to prevent haze formation. In this study, it is $54\ \mu g\ m^{-3}$.

Compared with those ($54–126\ \mu g\ m^{-3}$) during PLP, the PTV_{10} increased by $9–58\ \mu g\ m^{-3}$ ($p < 0.01$) for different RH ranges during LP. In other words, the visibilities were higher in LP than those for PLP under the same RH and $PM_{2.5}$ concentration. Moreover, the elevations in PTV_{10} implied that the reductions in $PM_{2.5}$ and RH could not thoroughly explain the increase in visibility. Other parameters including mass scattering efficiency (MSE), mass absorption efficiency (MAE), and optical hygroscopicity ($f(RH)$) for $PM_{2.5}$ should be also considered. In Fig. 2b, $PM_{2.5}$ was highly correlated with b_{sp} and b_{ap} ($R^2 \geq 0.58$, $p < 0.01$). The slopes of the linear regressions can be considered as the bulk MSE and MAE[38,42]. During LP, the MSE decreased by ~5% ($0.26\ m^2\ g^{-1}$) compared with that for PLP. While due to the aerosol aging[64], MAE raised by 24% ($0.06\ m^2\ g^{-1}$), partly counteracting the MSE reduction. However, compared with the decrease in MSE, the decrements in $f(RH)$ were more obviously as 6–14% ($p < 0.01$) for various RH ranges from PLP (1.57–3.46) to LP (1.48–3.12) (Fig. 2c). Since the ambient visibility was highly sensitive to $f(RH)$ changes under high RH conditions[19], the decline in $f(RH)$ was one of the key reasons for the increase of PTV_{10}. It is worth noting that the hygroscopic behavior of SOA has not been considered due to its minor contributions to b_{sp} and $f(RH)$.

The driver for ambient visibility improvement
The MSEs and MAEs of major chemical components in $PM_{2.5}$ were estimated by multiple linear regression (MLR) (Supplementary Table 1). The MSEs for NH_4NO_3 varied slightly from $5.9\ m^2\ g^{-1}$ for PLP to $4.2\ m^2\ g^{-1}$ for LP, while the values for $(NH4)_2SO_4$ changed dramatically from 1.2 to $4.4\ m^2\ g^{-1}$. These MSEs were comparable to the values of $1.7–17.4\ m^2\ g^{-1}$[65,66] for NH_4NO_3 and $1.9–9.2\ m^2\ g^{-1}$[23,67] for $(NH4)_2SO_4$ in previous studies, which are summarized in Supplementary Table 2. For $(NH_4)_2SO_4$ and NH_4NO_3, the variations in MSEs are related to particle size distribution, with particles in droplet mode (600–700 nm) holding the highest values[23,68,69]. The large increase in the MSE for $(NH4)_2SO_4$ was likely due to the fact that its particle size increased and approached to droplet mode during the aerosol aging processes as the COVID-19 lockdown significantly reduced primary emissions[45,59,61]. For primary organic aerosol (POA), the calculated MSEs ($8.4–9.3\ m^2\ g^{-1}$) were within the range of $1.0–16.7\ m^2\ g^{-1}$[67,70] (Supplementary Table 2). The MSEs for SOA, varying from $0.3\ m^2\ g^{-1}$ for PLP to $2.6\ m^2\ g^{-1}$ for LP, were lower than those for POA. They were also acceptable when compared with the values ($1.1–8.5\ m^2\ g^{-1}$[71]) in the former studies (Supplementary Table 2) though the MSE estimation of SOA for PLP did not pass the significance test ($p = 0.17$, Supplementary Table 1). From Supplementary Table 2, the MSEs for POA and SOA do not show necessarily high or low relationships as they are determined by the integral effects of mass concentrations, size distributions, emission sources, and morphology[72,73]. The increment in MSE for SOA might be associated with the variation in emission sources and the enlargement in particle size during LP. The MAEs for EC increased from $11.6\ m^2\ g^{-1}$ for PLP to $12.1\ m^2\ g^{-1}$ for LP due to the aerosol aging and were consistent with $7–14\ m^2\ g^{-1}$[66,74]. MAE of EC depends on its size distribution and coating[64]. It is noteworthy that there are no studies reporting MSEs of POA and SOA in $PM_{2.5}$ for comparison.

From Fig. 1c, NH_4NO_3 contributed the highest fractions to b_{ext} by 61.8% and 31.8% for the PLP and LP, respectively. Then POA (22.1 and 28.1%, respectively) and $(NH_4)_2SO_4$ (6.0 and 25.6%, respectively) followed. Other chemical species contributed < 7%. The estimated b_{ext} contributed from all chemical species
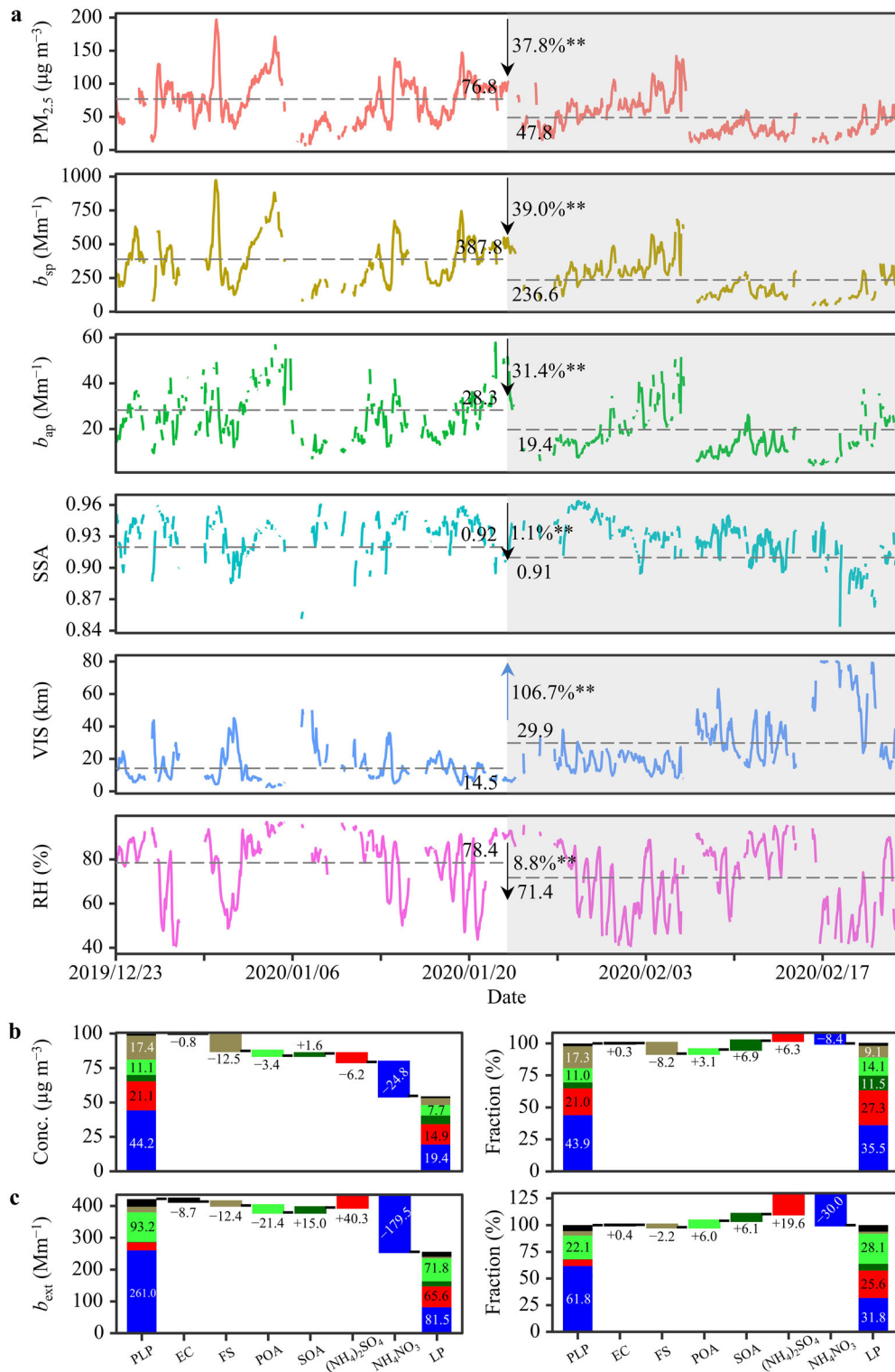
Fig. 1 Variations in PM$_{2.5}$ and ambient visibility between PLP and LP. a Time series of PM$_{2.5}$, aerosol scattering coefficient (b_{sp}), aerosol absorption coefficient (b_{ap}), single scattering albedo (SSA), ambient visibility (VIS), and relative humidity (RH) for pre-lockdown period (PLP, 2019/12/23–2020/01/22) and lockdown period (LP, 2020/01/23–2020/02/22) in Wuhan. The dashed lines mean the average value; **$p < 0.01$. **b** The differences in the mass concentrations and fractions of major chemical components in PM$_{2.5}$ for PLP and LP. **c** The differences in the contributions of major chemical components in PM$_{2.5}$ to aerosol extinction coefficient (b_{ext}) for PLP and LP. EC elemental carbon, POA primary organic aerosol, SOA secondary organic aerosol, FS fine soil.
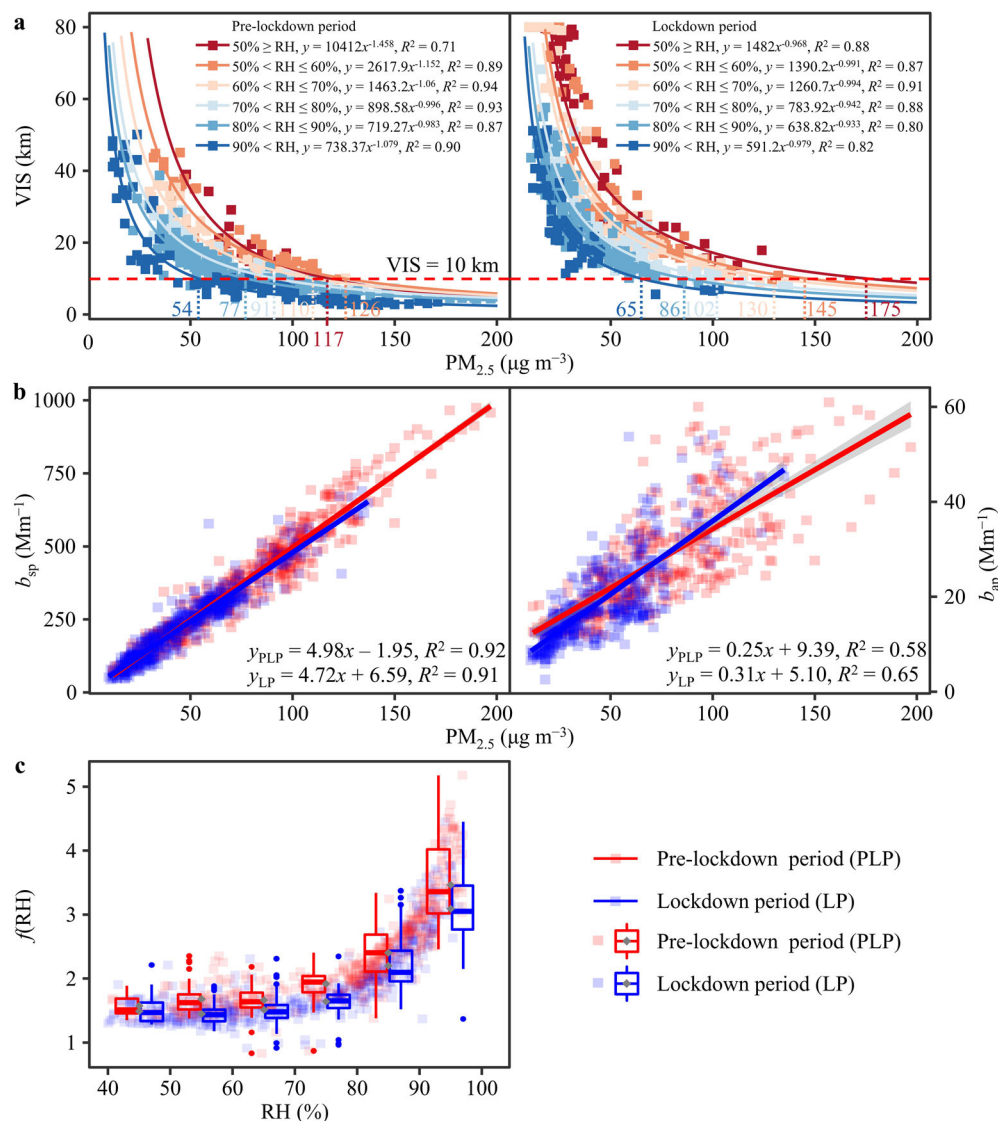
Fig. 2 Drivers for the elevations in PTV$_{10}$. a Scatter plots of ambient visibility (VIS) and PM$_{2.5}$ mass concentrations under different relative humidity (RH) ranges. The curves represent the fitting lines. **b** Scatter plots of aerosol scattering (b_{sp}) and absorption (b_{ap}) coefficients versus PM$_{2.5}$ mass concentrations. The gray zones represent the 95% confidence intervals. **c** Relationships between the optical hygroscopicity (f(RH)) of PM$_{2.5}$ and RH. The upper and lower boundaries of boxes (**c**) represent the 75th and 25th percentiles, respectively; the lines with the boxes mark the median; the whiskers above and below boxes indicate the maximum and minimum values, respectively; the diamonds along the boxes represent the average values; the dots indicate the potential outliers.

decreased by 8.7–179.5 Mm^{-1} during LP compared with those for PLP, except for (NH$_4$)$_2$SO$_4$ and SOA. As the decreases in the mass concentration (56.1%) and MSE (28.8%), NH$_4$NO$_3$ held the highest b_{ext} reduction and its contribution to b_{ext} displayed a decrease of 30%, which actuated the visibility improvement during LP. Liu et al.[16] found that from 2013 to 2017 the increased contributions of nitrate to particle mass and b_{ext} elevated the f(RH) and mass extinction efficiency of PM$_{2.5}$ in Eastern China, which hindered the visibility improvement. From PLP to LP, the estimated b_{ext} of SOA and (NH$_4$)$_2$SO$_4$ increased by 15.0 and 40.3 Mm^{-1}, although the mass concentration of (NH$_4$)$_2$SO$_4$ decreased by 29.4%. It indicated that the reduction strategies of PM$_{2.5}$ and associated chemical components currently in China would not reduce b_{ext} and improve the ambient visibility necessarily. A significant cutting down of NH$_4$NO$_3$ and its precursor (NO$_x$ or NH$_3$) can serve as the most effective way to improve ambient visibility in the future.

Weakened mutual promotion between AWC and NH$_4$NO$_3$
Previous studies revealed the vital role of aerosol composition alterations on hygroscopicity and b_{ext}[16,19,75,76]. The b_{ext} induced by aerosol hygroscopicity (Δb_{ext}) was estimated, which was the difference between the ambient and measured b_{ext}. In Fig. 3a, the Δb_{ext} and aerosol water content (AWC) displayed a similar temporal pattern and decreased by ~60% from PLP to LP averagely. The AWC was significantly ($p < 0.01$) correlated with Δb_{ext} ($R^2 = 0.86$) and ambient visibility ($R^2 = 0.72$) (Fig. 3b), indicating that the reduction in AWC would be another reason for improving ambient visibility. Besides the decreases in ambient RH and PM$_{2.5}$, 5.0–22.4 and 4.1–37.1% of the reductions in Δb_{ext} and AWC could be ascribed to the aerosol composition variations, respectively (Fig. 4).

NH$_4$NO$_3$ and (NH$_4$)$_2$SO$_4$ are the main hygroscopic compounds in aerosols and their abilities of water uptake are comparable with the same particle size and RH[33,77,78]. However, compared to (NH$_4$)$_2$SO$_4$ (80% at 298 K), NH$_4$NO$_3$ has a lower deliquescence RH

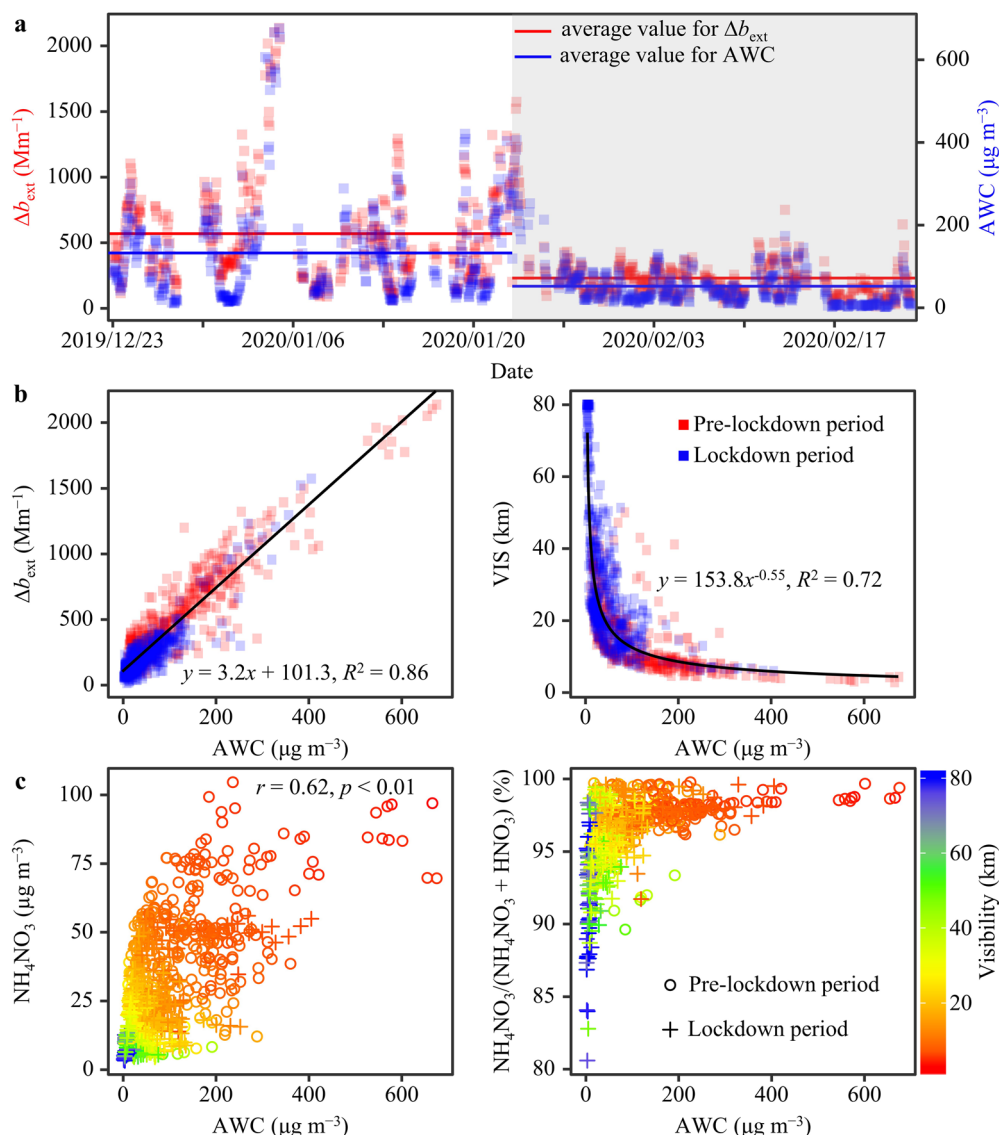**Fig. 3 Mechanisms for the further improvement of ambient visibility. a** Time series of the aerosol water content (AWC) and the differences (Δb_{ext}) between ambient and measured b_{ext}. **b** Scatter plots of AWC versus Δb_{ext} and visibility (VIS). **c** Scatter plots of AWC versus NH_4NO_3 concentration and the mass ratio of $NH_4NO_3/(NH_4NO_3 + HNO_3)$. The circles and crosses are colored based on ambient visibility.

(62% at 298 K)[77] and is more easily liquefied[79]. Following the method in Liu et al.[16] and Wexler and Seinfeld[80], the average $PM_{2.5}$ deliquescence humidity for LP (71.3%) was significantly ($p <$ 0.01) higher than that for PLP (70.0%) as the decrease in NH_4NO_3 mass percentage (Supplementary Fig. 2). It means higher ambient RH requirement for hygroscopic growth[16]. In addition, the aerosol water facilitates NH_4NO_3 formation[81–83] and the enhanced NH_4NO_3 fraction will promote water uptake correspondingly[33,84,85]. Such mutual promotion between the aerosol water and NH_4NO_3 degraded ambient visibility effectively (Fig. 3c), while the decreases in NH_4NO_3 and RH weakened the promotion and then reduced AWC and Δb_{ext}, which further improved the ambient visibility during LP.

Priority policies for co-regulating $PM_{2.5}$ and visibility

Reducing NH_4NO_3 can substantially reduce $PM_{2.5}$ and improve ambient visibility. This can be realized by reducing NO_x to lower HNO_3, which further transfers to particle phase, or reducing NH_3 to lower aerosol pH and keep HNO_3 in the gas phase[86]. In Fig. 5, all variables responded to NH_x ($NH_3 + NH_4^+$) reduction nonlinearly.

They flattened out until 36% (9.2 μg m^{-3}) and 43% (6.9 μg m^{-3}) NH_x reductions achieved for PLP and LP, respectively, at which points they started to decrease rapidly. The sweet spots for NH_x reduction (36 and 43%) were determined by a critical pH of 3, which balanced the partition between HNO_3 and NO_3^- [86]. It increased by 7% (Fig. 5a) due to the reductions of TNO_3 ($NO_3^- + HNO_3$) and SO_4^{2-} converting more NH_x into gas phase during LP[87], reflecting that the ambient visibility improvement would become more difficult via NH_x control. Fu et al.[88] also reported that increases in free NH_3 concentration could decrease the sensitivity of $PM_{2.5}$ reduction to NH_x emission control.

The impacts of reducing TNO_3 showed different responses. Decreasing TNO_3 did not obviously change pH due to the buffering by NH_3-NH_4^+ partitioning[86,89]. While the pH decreased clearly when NH_x reduction exceeded its sweet spots due to the increase of TNO_3 partitioning to HNO_3, the decrease of AWC, and the increase of hydrogen ion concentration in aerosol water[87]. A linear reduction in TNO_3 caused a linear decrease in $[NH_4^+ + NO_3^-]$ as the NO_3^- was nearly equal to TNO_3 (Fig. 5c). Then the decrease in TNO_3 was transmitted directly to $[NH_4^+ + NO_3^-]$[86]. Thus, controlling TNO_3 was a more direct and effective way to

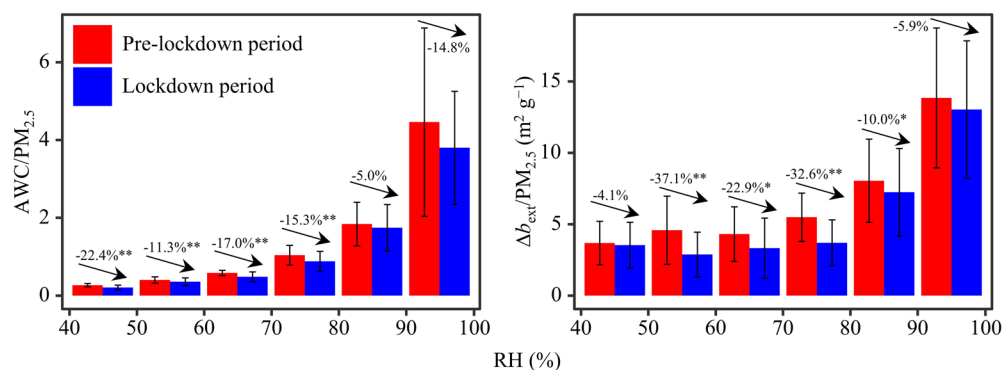**Fig. 4 Roles of aerosol composition variations on AWC and Δb_{ext}.** Comparisons of the normalized aerosol water content (AWC/PM$_{2.5}$) and the differences (Δb_{ext}) between ambient and measured b_{ext} (Δb_{ext}/PM$_{2.5}$) for pre-lockdown period and lockdown period under various relative humidity (RH) ranges. *$p < 0.05$; **$p < 0.01$. The error bar represents one standard deviation.
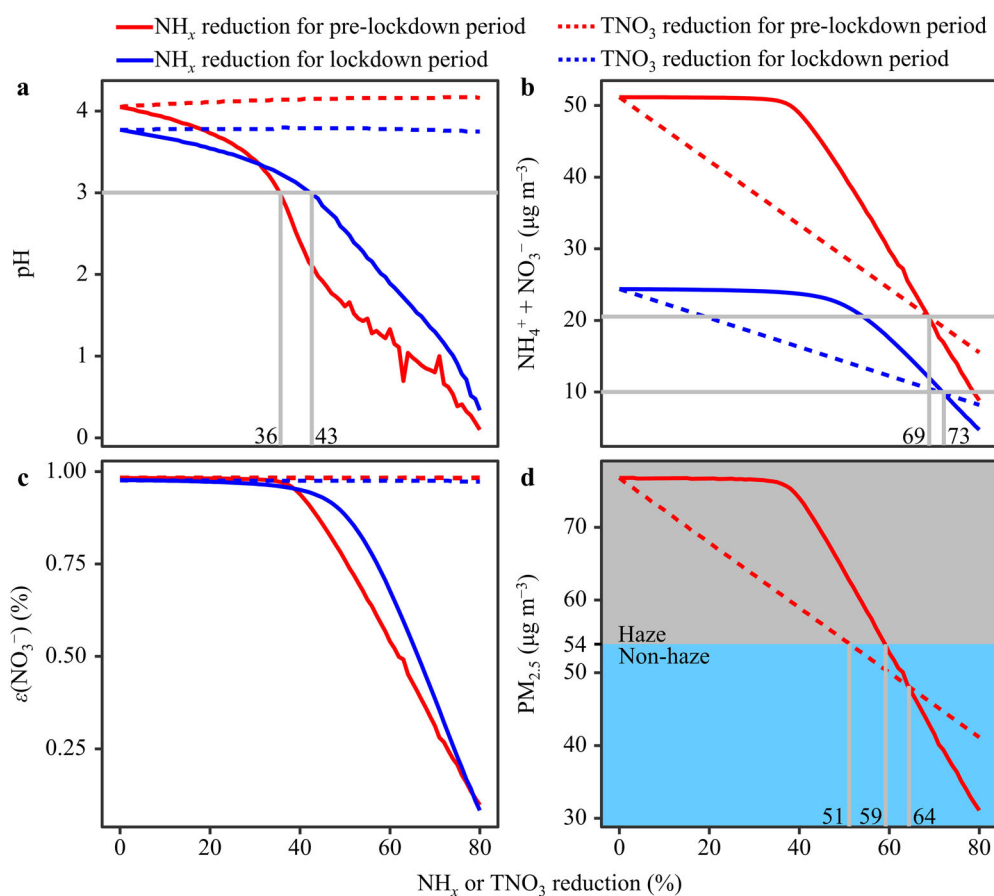

Fig. 5 Relative merits of NH$_x$ and TNO$_3$ controls on various aspects of PM$_{2.5}$. Aerosol pH (**a**), mass concentration of [NH$_4^+$ + NO$_3^-$] (**b**), proportion of particle nitrate (ε(NO$_3^-$)) (**c**), and PM$_{2.5}$ mass concentration (**d**) predicted by ISORROPIA-II model. The simulations are based on the average values, with changes only from NH$_x$ or TNO$_3$. The horizontal gray solid line in **a** identifies the critical pH value of 3[86].

elevate ambient visibility than NH$_x$. However, if the NH$_x$ reduction surpassed 69% (17.5 μg m^{-3}) and 73% (11.7 μg m^{-3}) for PLP and LP, respectively (Fig. 5b), it would become more effective in increasing ambient visibility than TNO$_3$ reduction. Wu et al.[90] suggested that the measures to reduce NH$_x$ pollution should be focused on non-agricultural emission sources in both local and surrounding areas of urban regions as the NH$_x$ emitted from agricultural sources has been highly overrated[90,91].

For guaranteeing blue sky in the future, the responses of average PM$_{2.5}$ concentration for PLP to NH$_x$ or TNO$_3$ reduction were roughly simulated given that the anthropogenic emissions have rebounded to pre-pandemic levels after Wuhan reo-pened[45,48]. A reduction of 51% in TNO$_3$ (17.9 μg m^{-3}) or 59% in NH$_x$ (15.0 μg m^{-3}) could make the PM$_{2.5}$ concentration < 54 μg m^{-3} and ensure the ambient visibility > 10 km (Fig. 5d). When the NH$_x$ reduction exceeded 64% (16.3 μg m^{-3}), it might be more effective in improving ambient visibility than TNO$_3$ reduction. The simultaneous reductions of NH$_x$ and TNO$_3$ with different ratios did not decrease their reduction threshold percentages corresponding to PM$_{2.5}$ of 54 μg m^{-3} (Fig. 6), which meant that just control TNO$_3$ was enough for improving ambient visibility. However, there are other welfares to control NH$_x$ emissions, for instance, reducing
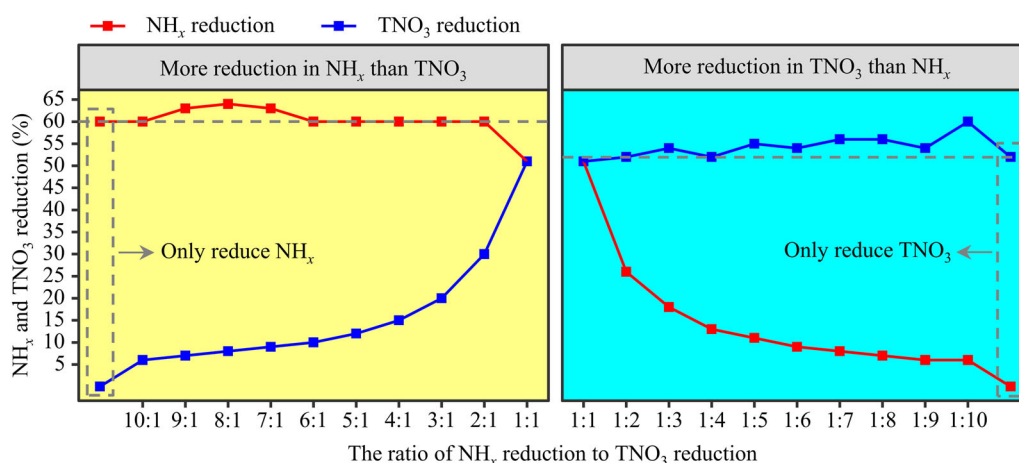
Fig. 6 Effects of simultaneous reductions of NH_x and TNO_3. The reduction threshold percentages of NH_x and TNO_3 corresponding to average $PM_{2.5}$ mass concentration of 54 $\mu g\,m^{-3}$ predicted by ISORROPIA-II model. The simulations are based on the average values for pre-lockdown period, with proportional changes from NH_x and TNO_3.
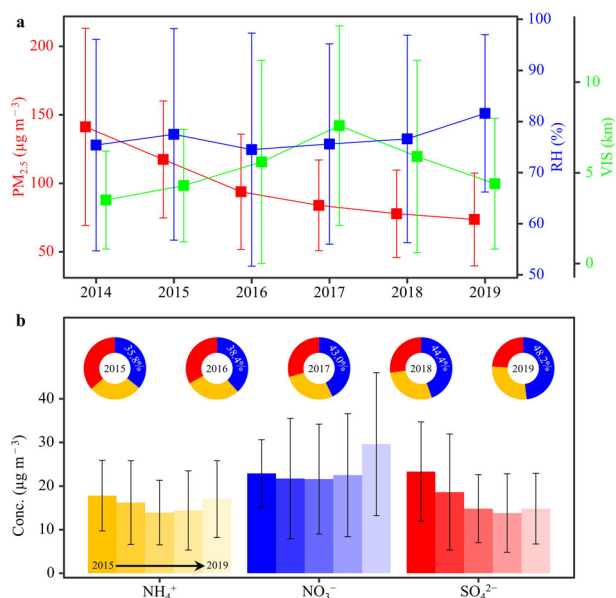

Fig. 7 Unsatisfactory visibility improvement along with steady increases in nitrate fractions. a Interannual trends in $PM_{2.5}$ concentration, relative humidity (RH), and ambient visibility (VIS) in Wuhan during 2014–2019 wintertime (January and February). **b** Interannual trends in NH_4^+, NO_3^-, and SO_4^{2-} concentrations and their contributions to SNA for $PM_{2.5}$ during 2015–2019 wintertime (January and February). The error bar represents one standard deviation.

nitrogen deposition and minimizing eutrophication in aqueous system[92]. Thus, multi-pollutant control but more priority given to TNO_3 reduction is proposed from the view of improving ambient visibility in China.

Since the secondary transformation has not been considered in the thermodynamic model, how to reduce TNO_3 and NH_x to certain concentrations by controlling their corresponding precursors (NO_x and NH_3) needs more in-depth studies. Cutting down the TNO_3 only via abating NO_x emissions should be treated with cautions as decreasing NO_x emissions may increase ozone and hydroxyl radical concentrations, which can enhance the conversion efficiency of NO_x to HNO_3 and then subdue the response of TNO_3 to NO_x emission reductions in the volatile organic compound (VOC)-limited ozone formation regime[18,93]. The

increased photochemical oxidants were the major drivers for persistent heavy nitrate pollution in winter in North China Plain[93]. It should be noted that Wuhan is also in a VOC-limited ozone formation regime[94].

Implications

To tackle the haze pollution, the Chinese government has implemented toughest ever emission control measures since 2013[13]. Consequently, the anthropogenic emissions of NH_3, NO_x, $PM_{2.5}$, and SO_2 in Hubei province decreased by 7.8–70.0% from 2013 to 2017 (Supplementary Fig. 3a). The SO_2 and NO_2 concentrations in Wuhan reduced by 84.0 and 27.9% from 2014 to 2019, respectively (Supplementary Fig. 3b). The $PM_{2.5}$ mass concentrations continually dropped by half from 141.2 to 73.6 $\mu g\,m^{-3}$ during the 2014–2019 wintertime (Fig. 7a). However, the air quality improvement might not be sensed by the public since the average ambient visibility was less improved and still remained < 10 km (Fig. 7a), which obscured the efforts government paid to alleviate the air pollution. Though RH could also diminish the sky[16,19], it was not the main reason curbing ambient visibility elevation as it displayed small fluctuations and no obvious variation was observed during 2014–2018 wintertime (Fig. 7a). The sharp decrease of ambient visibility in 2019 wintertime could be partly explained by the moderate increase in RH. The non-linear responses of visibility to $PM_{2.5}$ could also explain its unsatisfactory improvement. In Fig. 2a, the ambient visibility showed decreasing sensitive to $PM_{2.5}$ decrement with the aggravation of air pollution especially when the $PM_{2.5}$ concentrations were higher than the PTV_{10}. Thus, the large abatements in $PM_{2.5}$ mass concentrations during 2014–2019 wintertime did not bring about the huge improvement in ambient visibility as they were still > 54 $\mu g\,m^{-3}$, which pointed out the importance of establishing a strict hourly $PM_{2.5}$ standard. The great ambient visibility improvement appearing in LP can be expected in the future with the decrease of $PM_{2.5}$ when it is below the standard.

Such frustrating visibility improvement in Wuhan is not a particular case, which has been also found in Eastern China[16] and Southern China[19]. Even worse, it is likely to be widespread in China as Liu et al.[16] has demonstrated that nearly 73.2% stations across the country exhibited increasing slopes of AOD/$PM_{2.5}$ from 2013 to 2018. That is to say, though the $PM_{2.5}$ mass concentration has been substantially reduced, the increase of AOD per unit $PM_{2.5}$ indicated the less improved ambient visibility. Emission controls successfully brought down the loads of primary $PM_{2.5}$[15] and inevitably reduced its b_{ext}[19], while most of the visibility

improvement benefits raised by PM$_{2.5}$ reduction were balanced out by the elevation in aerosol optical hygroscopicity[16,19]. This increment was associated with the elevated proportions of NH$_4$NO$_3$ in PM$_{2.5}$ mass and b$_{ext}$[16]. Indeed, (NH$_4$)$_2$SO$_4$ typically dominated b$_{ext}$ (~40%) in the past decade[36], while the distinct emission controls of SO$_2$ and NO$_x$ resulted in a larger reduction in sulfate than in nitrate in China from 2013 to 2017[17,93,95]. Instead, nitrate is more important than sulfate as a driver for ambient visibility impairment[96,97]. Similarly, the nitrate mass concentration and its contribution to SNA have gradually increased during 2015–2019 wintertime in Wuhan despite the tremendous mitigation of PM$_{2.5}$ pollution (Fig. 7b). The evidently increased nitrate proportions would directly trigger the decrease in PM$_{2.5}$ deliquescence humidity[16]. It meant that a lower ambient RH was required for aerosol hygroscopic growth, which hindered the visibility improvement in Wuhan during wintertime.

Based on a positive example induced by the unexpected COVID-19 pandemic, this study reveals the co-benefits of reducing PM$_{2.5}$ and improving ambient visibility by cutting down NH$_4$NO$_3$. Reducing NH$_4$NO$_3$ will increase deliquescence humidity and decrease optical hygroscopicity, which can maximize the efficiency of decreasing PM$_{2.5}$ on improving ambient visibility under current air pollution condition. The recommendations for reducing PM$_{2.5}$ and improving visibility in a short term by reducing more TNO$_3$ than NH$_x$ are proposed. To resolve haze once and for all, the joint control of the two pollutants will gain other more welfares. It must be noted that wiping out the haze is not the terminus. The average PM$_{2.5}$ concentrations during LP still remained four times higher than the World Health Organization recommendations. Secondary inorganic aerosol (45.6%) and biomass burning (26.8%) were still the largest contributors to PM$_{2.5}$ (Supplementary Fig. 4) though the masses they contributed both decreased during LP, which needed further reductions. As shown in Supplementary Fig. 5, these contributions were both enhanced by the air masses transported from Eastern China[56], suggesting the necessity of regional-joint control.

METHODS

Observation

The sampling site (114.28°E, 30.6°N, Supplementary Fig. 6) is in a mixed residential and commercial area with no obvious industrial emissions. Hourly PM$_{10}$ and PM$_{2.5}$ dry mass concentrations were monitored by the oscillating balance method (TH, model: 2000Z, China)[63] during PLP (23 December 2019–22 January 2020) and LP (23 January 2020–22 February 2020). CO, NO$_x$ (NO + NO$_2$), O$_3$, and SO$_2$ (Supplementary Fig. 7) were hourly measured with a correlation infrared absorption analyzer (TAPI, model: 300E, USA), a chemiluminescence trace level NO–NO$_2$–NO$_x$ analyzer (Casella, model: ML9841B, UK), an ultraviolet (UV) photometric O$_3$ analyzer (TEI, model: 49i, USA), and a pulsed UV fluorescence SO$_2$ analyzer (Casella, model: ML9850B, UK), respectively[56].

Water-soluble ions, including NH$_4$$^+$, Na$^+$, Mg^{2+}, K$^+$, Ca^{2+}, Cl$^-$, NO$_3$$^-$, and SO$_4$$^{2-}$, and gaseous HNO$_3$, HCl, and NH$_3$ (Supplementary Fig. 7) were hourly detected using an online ion chromatograph (MARGA-1S, Switzerland). Hourly organic carbon and EC were monitored by a sunset OC/EC online analyzer (Model RT-4, Sunset Laboratory Inc., Tigard, OR, USA)[98]. Hourly trace elements were measured by a Xact multi-metal monitor (Model XactTM 625, Cooper Environmental Services, USA)[99].

Meteorological parameters, including atmospheric pressure, ambient temperature, RH, wind speed, and wind direction, were obtained by an automatic meteorological observation instrument (WS6000-UMB, Luff, Germany) with 1-h resolution. Hourly precipitation was provided by local meteorological administration. Ambient visibility was measured with a visibility monitor (Belfort Model 6000, USA) with ±10% of uncertainty. The mixing layer height was derived from the HYSPLIT model[56]. The time series of meteorological parameters are displayed in Supplementary Fig. 8.

The dry b$_{sp}$ at 525 nm was measured using an integrating Nephelometer (Aurora-1000, Ecotech, Australia) with RH of inflow air heated to <40%. The b$_{ap}$ at 532 nm was converted by the concentration of black carbon measured at 880 nm with an Aethalometer (Magee Scientific Company, Berkeley, CA,

USA, Model AE-31). The converted coefficient was 8.28 m^2 g^{-1}[100]. To match the b$_{sp}$ at 525 nm, the b$_{ap}$ at 532 nm was converted as referred to Nessler et al.[101]. The verification and calibration of the Nephelometer and Aethalometer can be found in Cao et al[22]. and Tao et al[65]. The single scattering albedo was calculated as the ratio of b$_{sp}$ to b$_{ext}$.

Data analysis

Fog, rain, and dust can reduce the atmospheric visibility. The datasets with RH > 97% was excluded to eliminate the effects of fog[19]. Data collected in the occurrence of precipitation were removed[63]. When the PM$_{2.5}$/PM$_{10}$ ratio was < 30%, the data were excluded as they might be impacted by long-range transport dust[63,102,103]. The hourly data were deleted if PM$_{2.5}$ concentrations were higher the PM$_{10}$ concentrations. Totally, the eliminated data accounted for 20% of the whole data.

The measured PM$_{2.5}$ was reconstructed by the sum of (NH$_4$)$_2$SO$_4$, NH$_4$NO$_3$, OM, EC, and fine soil[104]. The minimum R-Squared method[105] and a constant converting factor were used to divide OM into POA and SOA[24,59]. The MSEs for above chemical components expect for EC were estimated by MLR[41,66,106,107]. The MAEs for EC were estimated based on the scatter plots of EC against b$_{ap}$[24,41]. Statistics of MSEs and MAEs are presented in Supplementary Table 1. The bulk f(RH) for PM$_{2.5}$ was the ratio of estimated ambient b$_{sp}$ to corresponding measurements[19,35,108]. The thermodynamic model ISOROPPIA-II[109,110] was run with "forward mode" to calculate the AWC and to conduct sensitivity tests[86,87,111]. Positive matrix factorization (PMF 5.0) was employed to identify the sources of PM$_{2.5}$[24,38,56]. More details about the data processing are listed in Supplementary Methods. The glossaries of abbreviations are provided in Supplementary Table 3.

REFERENCES

1. Jacob, D. *Introduction to Atmospheric Chemistry* (Princeton Univ. Press, 1999).
2. Che, H., Zhang, X., Li, Y., Zhou, Z. & Qu, J. Horizontal visibility trends in China 1981–2005. *Geophys. Res. Lett.* **34**, L24706 (2007).
3. Chen, X. et al. Effects of human activities and climate change on the reduction of visibility in Beijing over the past 36 years. *Environ. Int.* **116**, 92–100 (2018).
4. Wang, K., Dickinson, R. & Liang, S. Clear sky visibility has decreased over land globally from 1973 to 2007. *Science* **323**, 1468–1470 (2009).
5. Zhang, S., Wu, J., Fan, W., Yang, Q. & Zhao, D. Review of aerosol optical depth retrieval using visibility data. *Earth Sci. Rev.* **200**, 102986 (2020).
6. Theofilatos, A. & Yannis, G. A review of the effect of traffic and weather characteristics on road safety. *Accid. Anal. Prev.* **72**, 244–256 (2014).
7. Zheng, S., Wang, J., Sun, C., Zhang, X. & Kahn, M. Air pollution lowers Chinese urbanites' expressed happiness on social media. *Nat. Hum. Behav.* **3**, 237–243 (2019).
8. An, Z. et al. Severe haze in northern China: a synergy of anthropogenic emissions and atmospheric processes. *Proc. Natl Acad. Sci. USA* **116**, 8657–8666 (2019).
9. Guo, S. et al. Elucidating severe urban haze formation in China. *Proc. Natl Acad. Sci. USA* **111**, 17373–17378 (2014).
10. Huang, R. et al. High secondary aerosol contribution to particulate pollution during haze events in China. *Nature* **514**, 218–222 (2014).
11. Huang, X. et al. Amplified transboundary transport of haze by aerosol-boundary layer interaction in China. *Nat. Geosci.* **13**, 428–434 (2020).
12. Zhang, F. et al. An unexpected catalyst dominates formation and radiative forcing of regional haze. *Proc. Natl Acad. Sci. USA* **117**, 3960–3966 (2020).
13. China State Council. Action plan on prevention and control of air pollution (in Chinese). http://www.gov.cn/zwgk/2013-09/12/content_2486773.htm (2013).
14. Ding, A. et al. Significant reduction of PM$_{2.5}$ in eastern China due to regional-scale emission control: evidence from SORPES in 2011–2018. *Atmos. Chem. Phys.* **19**, 11791–11801 (2019).
15. Zhang, Q. et al. Drivers of improved PM$_{2.5}$ air quality in China from 2013 to 2017. *Proc. Natl Acad. Sci. USA* **116**, 24463–24469 (2019).
16. Liu, J. et al. Increased aerosol extinction efficiency hinders visibility improvement in Eastern China. *Geophys. Res. Lett.* **47**, e2020GL090167 (2020).

17. Zheng, B. et al. Trends in China's anthropogenic emissions since 2010 as the consequence of clean air actions. *Atmos. Chem. Phys.* **18**, 14095–14111 (2018).

18. Huang, X. et al. Enhanced secondary pollution offset reduction of primary emissions during COVID-19 lockdown in China. *Natl. Sci. Rev.* **8**, nwaa137 (2020).

19. Xu, W. et al. Current challenges in visibility improvement in Southern China. *Environ. Sci. Technol. Lett.* **7**, 395–401 (2020).

20. National Bulletin of Atmospheric Environment (in Chinese). Meteorological bulletin of the atmospheric environment (2018 edition). http://www.nmc.cn/publish/environment/National-Bulletin-atmospheric-environment.htm (2019).

21. Chow, J. et al. Visibility: science and regulation. *J. Air Waste Manag.* **52**, 973–999 (2002).

22. Cao, J. et al. Impacts of aerosol compositions on visibility impairment in Xi'an, China. *Atmos. Environ.* **59**, 559–566 (2012).

23. Tao, J. et al. Impact of particle number and mass size distributions of major chemical components on particle mass scattering efficiency in urban Guangzhou in southern China. *Atmos. Chem. Phys.* **19**, 8471–8490 (2019).

24. Wang, Q. et al. Impacts of short-term mitigation measures on $PM_{2.5}$ and radiative effects: a case study at a regional background site near Beijing, China. *Atmos. Chem. Phys.* **19**, 1881–1899 (2019).

25. Zhang, Z., Shen, Y., Li, Y., Zhu, B. & Yu, X. Analysis of extinction properties as a function of relative humidity using a κ-EC-Mie model in Nanjing. *Atmos. Chem. Phys.* **17**, 4147–4157 (2017).

26. Tao, J. et al. Aerosol chemical composition and light scattering during a winter season in Beijing. *Atmos. Environ.* **110**, 36–44 (2015).

27. Yu, X. et al. Impacts of meteorological condition and aerosol chemical compositions on visibility impairment in Nanjing, China. *J. Clean. Prod.* **131**, 112–120 (2016).

28. Liao, W. et al. Characterization of aerosol chemical composition and the reconstruction of light extinction coefficients during winter in Wuhan, China. *Chemosphere* **241**, 125033 (2020).

29. Cheng, Y. et al. Reactive nitrogen chemistry in aerosol water as a source of sulfate during haze events in China. *Sci. Adv.* **2**, e1601530 (2016).

30. Xue, J. et al. Efficient control of atmospheric sulfate production based on three formation regimes. *Nat. Geosci.* **12**, 977–982 (2019).

31. Wang, G. et al. Persistent sulfate formation from London fog to Chinese haze. *Proc. Natl Acad. Sci.* **113**, 13630–13635 (2016).

32. Wang, J. et al. Fast sulfate formation from oxidation of SO_2 by NO_2 and HONO observed in Beijing haze. *Nat. Commun.* **11**, 2844 (2020).

33. Wang, Y. et al. Mutual promotion between aerosol particle liquid water and particulate nitrate enhancement leads to severe nitrate-dominated particulate matter pollution and low visibility. *Atmos. Chem. Phys.* **20**, 2161–2175 (2020).

34. Chen, J., Zhao, C., Ma, N. & Yan, P. Aerosol hygroscopicity parameter derived from the light scattering enhancement factor measurements in the North China Plain. *Atmos. Chem. Phys.* **14**, 8105–8118 (2014).

35. Zhao, C., Yu, Y., Kuang, Y., Tao, J. & Zhao, G. Recent progress of aerosol light-scattering enhancement factor studies in China. *Adv. Atmos. Sci.* **36**, 1015–1026 (2019).

36. Tao, J., Zhang, L., Cao, J. & Zhang, R. A review of current knowledge concerning $PM_{2.5}$ chemical composition, aerosol optical properties and their relationships across China. *Atmos. Chem. Phys.* **17**, 9485–9518 (2017).

37. Xu, W. et al. Air quality improvement in a megacity: implications from 2015 Beijing Parade Blue pollution control actions. *Atmos. Chem. Phys.* **17**, 31–46 (2017).

38. Zhou, Y. et al. Optical properties of aerosols and implications for radiative effects in Beijing during the Asia-Pacific Economic Cooperation Summit 2014. *J. Geophys. Res. Atmos.* **122**, 10119–10132 (2017).

39. Wang, S. et al. Chinese blue days: a novel index and spatio-temporal variations. *Environ. Res. Lett.* **14**, 074026 (2019).

40. Li, X. et al. $PM_{2.5}$ mass, chemical composition, and light extinction before and during the 2008 Beijing Olympics. *J. Geophys. Res. Atmos.* **118**, 12158–12167 (2013).

41. Tao, J. et al. Chemical and optical characteristics of atmospheric aerosols in Beijing during the Asia-Pacific Economic Cooperation China 2014. *Atmos. Environ.* **144**, 8–16 (2016).

42. Tao, J. et al. Control of $PM_{2.5}$ in Guangzhou during the 16th Asian Games period: Implication for hazy weather prevention. *Sci. Total Environ.* **508**, 57–66 (2015).

43. Le Quéré, C. et al. Temporary reduction in daily global CO_2 emissions during the COVID-19 forced confinement. *Nat. Clim. Chang.* **10**, 647–653 (2020).

44. Liu, Z. et al. Near-real-time monitoring of global CO_2 emissions reveals the effects of the COVID-19 pandemic. *Nat. Commun.* **11**, 5172 (2020).

45. Zheng, B. et al. Satellite-based estimates of decline and rebound in China's CO_2 emissions during COVID-19 pandemic. *Sci. Adv.* **6**, eabd4998 (2020).

46. Bauwens, M. et al. Impact of coronavirus outbreak on NO_2 pollution assessed using TROPOMI and OMI observations. *Geophys. Res. Lett.* **47**, e2020GL087978 (2020).

47. Fan, C. et al. The impact of the control measures during the COVID-19 outbreak on air pollution in China. *Remote Sens.* **12**, 1613 (2020).

48. Zhang, Q. et al. Substantial nitrogen oxides emission reduction from China due to COVID-19 and its impact on surface ozone and aerosol pollution. *Sci. Total Environ.* **753**, 142238 (2021).

49. Li, L. et al. Air quality changes during the COVID-19 lockdown over the Yangtze River Delta Region: an insight into the impact of human activity pattern changes on air pollution variation. *Sci. Total Environ.* **732**, 139282 (2020).

50. Wang, Y. et al. Changes in air quality related to the control of coronavirus in China: implications for traffic and industrial emissions. *Sci. Total Environ.* **731**, 139133 (2020).

51. Yuan, Q. et al. Spatiotemporal variations and reduction of air pollutants during the COVID-19 pandemic in a megacity of Yangtze River Delta in China. *Sci. Total Environ.* **751**, 141820 (2021).

52. Chen, H. et al. Impact of quarantine measures on chemical compositions of $PM_{2.5}$ during the COVID-19 epidemic in Shanghai, China. *Sci. Total Environ.* **743**, 140758 (2020).

53. Sun, Y. et al. A chemical cocktail during the COVID-19 outbreak in Beijing, China: insights from six-year aerosol particle composition measurements during the Chinese New Year holiday. *Sci. Total Environ.* **742**, 140739 (2020).

54. Xu, L. et al. Variation in concentration and sources of black carbon in a megacity of China during the COVID-19 pandemic. *Geophys. Res. Lett.* **47**, e2020GL090444 (2020).

55. Xu, J. et al. COVID-19 impact on the concentration and composition of submicron particulate matter in a typical city of Northwest China. *Geophys. Res. Lett.* **47**, e2020GL089035 (2020).

56. Zheng, H. et al. Significant changes in the chemical compositions and sources of $PM_{2.5}$ in Wuhan since the city lockdown as COVID-19. *Sci. Total Environ.* **739**, 140000 (2020).

57. Le, T. et al. Unexpected air pollution with marked emission reductions during the COVID-19 outbreak in China. *Science* **369**, 702–706 (2020).

58. Shi, Z. et al. Abrupt but smaller than expected changes in surface air quality attributable to COVID-19 lockdowns. *Sci. Adv.* **7**, eabd6696 (2021).

59. Chang, Y. et al. Puzzling haze events in China during the coronavirus (COVID-19) shutdown. *Geophys. Res. Lett.* **47**, e2020GL088533 (2020).

60. Shen, L. et al. Importance of meteorology in air pollution events during the city lockdown for COVID-19 in Hubei Province, Central China. *Sci. Total Environ.* **754**, 142227 (2021).

61. Lv, Z. et al. Source-receptor relationship revealed by the halted traffic and aggravated haze in Beijing during the COVID-19 lockdown. *Environ. Sci. Technol.* **54**, 15660–15670 (2020).

62. Wang, H. et al. Aerosol optical properties and chemical composition apportionment in Sichuan Basin, China. *Sci. Total Environ.* **577**, 245–257 (2017).

63. Wang, X., Zhang, R. & Yu, W. The effects of $PM_{2.5}$ concentrations and relative humidity on atmospheric visibility in Beijing. *J. Geophys. Res. Atmos.* **124**, 2235–2259 (2019).

64. Wu, C., Wu, D. & Yu, J. Z. Quantifying black carbon light absorption enhancement with a novel statistical approach. *Atmos. Chem. Phys.* **18**, 289–309 (2018).

65. Tao, J. et al. Characterization and source apportionment of aerosol light extinction in Chengdu, southwest China. *Atmos. Environ.* **95**, 552–562 (2014).

66. Zhou, Y. et al. Exploring the impact of chemical composition on aerosol light extinction during winter in a heavily polluted urban area of China. *J. Environ. Manag.* **247**, 766–775 (2019).

67. Lan, Z. et al. Source apportionment of $PM_{2.5}$ light extinction in an urban atmosphere in China. *J. Environ. Sci.* **63**, 277–284 (2018).

68. Xia, Y. et al. Impact of size distributions of major chemical components in fine particles on light extinction in urban Guangzhou. *Sci. Total Environ.* **587–588**, 240–247 (2017).

69. Yao, L. et al. Optical properties closure and sources of size-resolved aerosol in Nanjing around summer harvest period. *Atmos. Environ.* **244**, 118017 (2021).

70. Wang, Q. et al. Chemical composition of aerosol particles and light extinction apportionment before and during the heating season in Beijing, China. *J. Geophys. Res. Atmos.* **120**, 12708–12722 (2015).

71. Han, T. et al. Chemical apportionment of aerosol optical properties during the Asia-Pacific Economic Cooperation summit in Beijing, China. *J. Geophys. Res. Atmos.* **120**, 12281–12295 (2015).

72. Zhu, W. et al. Reconstructed algorithm for scattering coefficient of ambient submicron particles. *Environ. Pollut.* **253**, 439–448 (2019).

73. Zhu, W. et al. A novel algorithm to determine the scattering coefficient of ambient organic aerosols. *Environ. Pollut.* **270**, 116209 (2021).

74. Xu, X. et al. Optical properties of atmospheric fine particles near Beijing during the HOPE-J³A campaign. *Atmos. Chem. Phys.* **16**, 6421–6439 (2016).

75. Kuang, Y. et al. Deliquescent phenomena of ambient aerosols on the North China Plain. *Geophys. Res. Lett.* **43**, 8744–8750 (2016).

76. Wang, Y. et al. Enhanced hydrophobicity and volatility of submicron aerosols under severe emission control conditions in Beijing. *Atmos. Chem. Phys.* **17**, 5239–5251 (2017).

77. Kreidenweis, S. & Asa-Awuku, A. Aerosol hygroscopicity: Particle water content and its role in atmospheric processes. *Treatise Geochem.* **5**, 331–361 (2014).

78. Wu, Z. et al. Particle hygroscopicity and its link to chemical composition in the urban atmosphere of Beijing, China, during summertime. *Atmos. Chem. Phys.* **16**, 1123–1138 (2016).

79. Li, Y., Liu, P., Bergoend, C., Bateman, A. & Martin, S. Rebounding hygroscopic inorganic aerosol particles: Liquids, gels, and hydrates. *Aerosol Sci. Technol.* **51**, 388–396 (2017).

80. Wexler, A. & Seinfeld, J. Second-generation inorganic aerosol model. *Atmos. Environ. Part A. Gen. Top.* **25**, 2731–2748 (1991).

81. Harrison, R., Sturges, W., Kitto, A. & Li, Y. Kinetics of evaporation of ammonium chloride and ammonium nitrate aerosols. *Atmos. Environ. A Gen. Top.* **24**, 1883–1888 (1990).

82. Meng, Z. & Seinfeld, J. Time scales to achieve atmospheric gas-aerosol equilibrium for volatile species. *Atmos. Environ.* **30**, 2889–2900 (1996).

83. Shi, Y. et al. Airborne submicron particulate (PM_1) pollution in Shanghai, China: chemical variability, formation/dissociation of associated semi-volatile components and the impacts on visibility. *Sci. Total Environ.* **473–474**, 199–206 (2014).

84. Langridge, J. et al. Evolution of aerosol properties impacting visibility and direct climate forcing in an ammonia-rich urban environment. *J. Geophys. Res. Atmos.* **117**, D00V11 (2012).

85. Morgan, W. et al. Airborne measurements of the spatial distribution of aerosol chemical composition across Europe and evolution of the organic fraction. *Atmos. Chem. Phys.* **10**, 4065–4083 (2010).

86. Guo, H. et al. Effectiveness of ammonia reduction on control of fine particle nitrate. *Atmos. Chem. Phys.* **18**, 12241–12256 (2018).

87. Zheng, M. et al. Initial cost barrier of ammonia control in Central China. *Geophys. Res. Lett.* **46**, 14175–14184 (2019).

88. Fu, X. et al. Increasing ammonia concentrations reduce the effectiveness of particle pollution control achieved via SO_2 and NO_X emissions reduction in East China. *Environ. Sci. Technol. Lett.* **4**, 221–227 (2017).

89. Weber, R., Guo, H., Russell, A. & Nenes, A. High aerosol acidity despite declining atmospheric sulfate concentrations over the past 15 years. *Nat. Geosci.* **9**, 282–285 (2016).

90. Wu, L. et al. Aerosol ammonium in the urban boundary layer in Beijing: Insights from nitrogen isotope ratios and simulations in summer 2015. *Environ. Sci. Technol. Lett.* **6**, 389–395 (2019).

91. Chang, Y. et al. Assessing contributions of agricultural and nonagricultural emissions to atmospheric ammonia in a Chinese megacity. *Environ. Sci. Technol.* **53**, 1822–1833 (2019).

92. Yu, G. et al. Stabilization of atmospheric nitrogen deposition in China over the past decade. *Nat. Geosci.* **12**, 424–429 (2019).

93. Fu, X. et al. Persistent heavy winter nitrate pollution driven by increased photochemical oxidants in Northern China. *Environ. Sci. Technol.* **54**, 3881–3889 (2020).

94. Yan, Y. et al. On the local anthropogenic source diversities and transboundary transport for urban agglomeration ozone mitigation. *Atmos. Environ.* **245**, 118005 (2021).

95. Xu, Q. et al. Nitrate dominates the chemical composition of $PM_{2.5}$ during haze event in Beijing, China. *Sci. Total Environ.* **689**, 1293–1303 (2019).

96. Li, H. et al. Nitrate-driven urban haze pollution during summertime over the North China Plain. *Atmos. Chem. Phys.* **18**, 5293–5306 (2018).

97. Li, H. et al. Rapid transition in winter aerosol composition in Beijing from 2014 to 2017: Response to clean air actions. *Atmos. Chem. Phys.* **19**, 11485–11499 (2019).

98. Lyu, X. et al. Chemical characteristics and causes of airborne particulate pollution in warm seasons in Wuhan, central China. *Atmos. Chem. Phys.* **16**, 10671–10687 (2016).

99. Chang, Y. et al. First long-term and near real-time measurement of trace elements in China's urban atmosphere: Temporal variability, source apportionment and precipitation effect. *Atmos. Chem. Phys.* **18**, 11793–11812 (2018).

100. Yan, P. et al. The measurement of aerosol optical properties at a rural site in Northern China. *Atmos. Chem. Phys.* **8**, 2229–2242 (2008).

101. Nessler, R., Weingartner, E. & Baltensperger, U. Effect of humidity on aerosol light absorption and its implications for extinction and the single scattering albedo illustrated for a site in the lower free troposphere. *J. Aerosol Sci.* **36**, 958–972 (2005).

102. Tong, D., Wang, J., Gill, T. E., Lei, H. & Wang, B. Intensified dust storm activity and valley fever infection in the southwestern United States. *Geophys. Res. Lett.* **44**, 4304–4312 (2017).

103. Wang, Y. et al. Spatial and temporal variations of the concentrations of PM_{10}, $PM_{2.5}$ and PM_1 in China. *Atmos. Chem. Phys.* **15**, 13585–13598 (2015).

104. Pitchford, M. et al. Revised algorithm for estimating light extinction from IMPROVE particle speciation data. *J. Air Waste Manag.* **57**, 1326–1336 (2007).

105. Wu, C. & Yu, J. Determination of primary combustion source organic carbon-to-elemental carbon (OC/EC) ratio using ambient OC and EC measurements: Secondary OC-EC correlation minimization method. *Atmos. Chem. Phys.* **16**, 5453–5465 (2016).

106. Hand, J. & Malm, W. Review of aerosol mass scattering efficiencies from ground-based measurements since 1990. *J. Geophys. Res.* **112**, D16203 (2007).

107. Han, T. et al. Aerosol optical properties measurements by a CAPS single scattering albedo monitor: Comparisons between summer and winter in Beijing, China. *J. Geophys. Res. Atmos.* **122**, 2513–2526 (2017).

108. Ding, J. et al. Comparison of size-resolved hygroscopic growth factors of urban aerosol by different methods in Tianjin during a haze episode. *Sci. Total Environ.* **678**, 618–626 (2019).

109. Fountoukis, C. & Nenes, A. ISORROPIA II: a computationally efficient thermodynamic equilibrium model for K^+-Ca_2^+-Mg_2^+-NH_4^+-Na^+-SO_4^{2-}-NO_3^--Cl^--H_2O aerosols. *Atmos. Chem. Phys.* **7**, 4639–4659 (2007).

110. Nenes, A., Pandis, S. N. & Pilinis, C. ISORROPIA: a new thermodynamic equilibrium model for multiphase multicomponent inorganic aerosols. *Aquat. Geochem.* **4**, 123–152 (1998).

111. Ding, J. et al. Aerosol pH and its driving factors in Beijing. *Atmos. Chem. Phys.* **19**, 7939–7954 (2019).

ACKNOWLEDGEMENTS

AUTHOR CONTRIBUTIONS

L.Y. analyzed the data and wrote the manuscript; S.K. designed the study, received the funding resources, and reviewed and edited the manuscript; N.C., B.Z., K.X., W.C., and Y.B. provided the dataset; H.Z., Y.Z., M.Z., Y.C., Y.H., and Z.Z. helped the data analysis; Y.Y., D.L., T.Z., and S.Q. edited the manuscript. All authors contributed to the discussion and revision.

COMPETING INTERESTS

The authors declare no competing interests.

ADDITIONAL INFORMATION

Supplementary information The online version contains supplementary material available at https://doi.org/10.1038/s41612-021-00195-6.

Correspondence and requests for materials should be addressed to S.K.

Reprints and permission information is available at http://www.nature.com/reprints

Publisher's note Springer Nature remains neutral with regard to jurisdictional claims in published maps and institutional affiliations.